frontiers | Frontiers in Materials

REVIEW
published: 11 April 2022
doi: 10.3389/fmats.2022.825276

Directed Energy Deposition of Multi-Principal Element Alloys

*Praveen Sreeramagiri and Ganesh Balasubramanian**

Department of Mechanical Engineering and Mechanics, Lehigh University, Bethlehem, PA, United States

As efforts associated with the exploration of multi-principal element alloys (MPEAs) using computational and data-intensive methods continue to rise, experimental realization and validation of the predicted material properties require high-throughput and combinatorial synthesis of these alloys. While additive manufacturing (AM) has emerged as the leading pathway to address these challenges and for rapid prototyping through part fabrication, extensive research on developing and understanding the process-structure-property correlations is imminent. In particular, directed energy deposition (DED) based AM of MPEAs holds great promise because of the boundless compositional variations possible for functionally graded component manufacturing as well as surface cladding. We analyze the recent efforts in DED of MPEAs, the microstructural evolution during the laser metal deposition of various transition and refractory elements, and assess the effects of various processing parameters on the material phase and properties. Our efforts suggest that the development of robust predictive approaches for process parameter selection and modifying the synthesis mechanisms are essential to enable DED platforms to repeatedly produce defect free, stable and designer MPEAs.

Keywords: multi-principal element alloys, directed energy deposition, laser metal deposition, grains, crack formation, melt pool

OPEN ACCESS

Edited by:
E-Wen Huang,
National Yang Ming Chiao Tung University, Taiwan

Reviewed by:
Amir Motallebzadeh,
Koç University, Turkey
David Keffer,
The University of Tennessee, United States

****Correspondence:***
Ganesh Balasubramanian
bganesh@lehigh.edu

Specialty section:
This article was submitted to Mechanics of Materials, a section of the journal Frontiers in Materials

Received: *30 November 2021*
Accepted: *08 February 2022*
Published: *11 April 2022*

Citation:
Sreeramagiri P and Balasubramanian G (2022) Directed Energy Deposition of Multi-Principal Element Alloys. Front. Mater. 9:825276. doi: 10.3389/fmats.2022.825276

MULTI-PRINCIPAL ELEMENT ALLOYS

Cantor et al. (Cantor et al., 2004) and Yeh et al. (Yeh et al., 2004) demonstrated a new strategy to design phase stable alloys focusing on the center of the phase diagram (**Figure 1**). This concept ushered a new dimension to alloying multiple principal elements that are mixed in notable proportions, yet producing single-phase solid-solutions. The genesis of multi-principal element alloys (MPEAs) since has inspired researchers worldwide to examine many of the potential 10^{78} elemental combinations that could be possibly realized (Cantor, 2014). A subset of MPEAs, the high-entropy alloy (HEA) refers to those that consist of five or more principal elements, each occupying relatively high concentrations (~5–35 at.%) in the alloy composition (**Figure 1**), and forming a single phase random solid-solution due to the enhanced configurational entropy (Yeh et al., 2004). The continued interest in MPEAs and HEAs can be attributed to the remarkable mechanical properties demonstrated by certain compositions, such as high yield strength at elevated temperature, superior hardness and creep resistance etc. relative to conventional dilute solid-solution and precipitation-strengthened alloys (Gludovatz et al., 2016; Singh et al., 2018; Rickman et al., 2019; Gianelle et al., 2020; Roy et al., 2020, 2021b; Khakurel et al., 2021). These underlying strengthening mechanisms for such intriguing properties are primarily ascribed to lattice strain, short-range order effects and sluggish diffusion (Senkov et al., 2010; Mishra et al., 2015; Sharma et al., 2016; Fernández-Caballero et al., 2017; Ding et al., 2018; Antillon et al., 2020; Roy et al., 2021a; Sreeramagiri et al., 2021), while high fatigue endurance limit and toughness are credited to the competing behavior of twins and

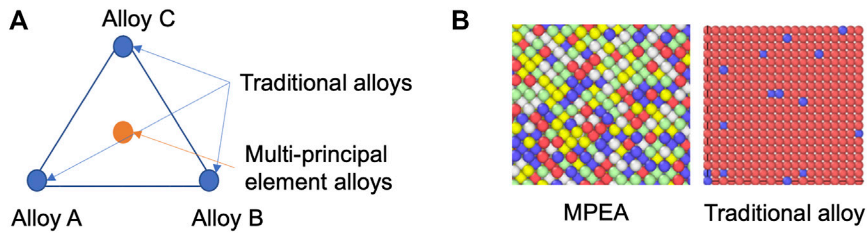

FIGURE 1 | Comparing dilute (conventional) and concentrated (MPEA) solid solutions: **(A)** In a ternary phase diagram conventional alloys are constrained to corners of the compositional space, whereas MPEAs occupy regions near the center of the phase diagram. **(B)** Random segregation of various elements can occur in MPEAs pertaining to a single phase solid-solution, while a sparse distribution of minor proportions of alloying elements is noted in conventional alloys.

dislocations (Mishra et al., 2015; Sharma et al., 2021). Interestingly, ternary (i.e., low entropy) alloys can possess a superior strength relative to the high-entropic quaternary or quinary counterparts when the former assumes a high lattice strain resulting from the difference of the atomic radii of constituent elements (Laplanche et al., 2017; Roy et al., 2021b). These findings further corroborated that the strengthening in MPEAs is predominantly driven by short range order and misfit strain energies between the different elements (Antillon et al., 2020).

A Case for High-Throughput Synthesis of MPEAs

The ever-increasing literature on MPEAs is still limited to extend across the enormous magnitude of realizable elemental combinations, and hence a large part of the compositional landscape remains to be explored. Data-intensive and theory-guided computational techniques, including CALPHAD (Kozeschnik and Buchmayr, 2001; Andersson et al., 2002; Saunders et al., 2003), first principles and atomistic methods (Plimpton, 1995; Kresse and Furthmüller, 1996; Kresse and Joubert, 1999), and machine learning (Sharma et al., 2017b; Roy et al., 2020, 2021b; Roy and Balasubramanian, 2021; Singh et al., 2021a, 2021b), have facilitated the interrogation of this vast compositional space to design and discover new MPEAs with targeted properties (Gao and Alman, 2013; Sharma et al., 2016, 2017a, 2017b, 2018; Haase et al., 2017; Sharma and Balasubramanian, 2017; Osei-Agyemang and Balasubramanian, 2019, 2021; Rickman et al., 2019, 2020; Singh et al., 2019, 2021a, 2021b; Johnson et al., 2020; Roy et al., 2021a, 2021b; Sreeramagiri et al., 2021; Roy and Balasubramanian, 2021). Nevertheless, the promising composition-structure-property predictions derived from such compute-intensive techniques require robust experimental validation, preferably through combinatorial and high-throughput syntheses (Singh et al., 2018; Roy et al., 2021b; Roy and Balasubramanian, 2021), such as metal additive manufacturing (AM), which has demonstrated its potential in alloy development (Dinda et al., 2008, 2009; Jia and Gu, 2014; Ramakrishnan and Dinda, 2019; Sreeramagiri et al., 2020b, 2020a). These manufacturing platforms can throttle the pace to screen numerous MPEA compositions within a fraction of the time invested towards traditional processes such as arc-melting (Huang et al., 2012a; Kunce et al., 2013, Kunce et al., 2014, 2015; Welk et al., 2013; Yue et al., 2014; Choudhuri et al., 2015, 2017; Sistla et al., 2015; Dobbelstein et al., 2016; Ocelík et al., 2016; Borkar et al., 2016; Wang et al., 2017; Joseph et al., 2017; Li et al., 2020b; Sreeramagiri et al., 2020b). Reducing the synthesis period to produce a population of MPEAs for experimental validation of the computational predictions will promote rapid scrutiny, discovery and development of novel alloys.

An Opportunity With Metal Additive Manufacturing

Additive manufacturing (AM) (a.k.a. 3D printing/solid free form fabrication) is the process of adding material layer by layer in accord with a computer aided design (CAD) to fabricate the desired component (Gibson et al., 2014; Wohlers and Tim, 2014). Since the commercialization of the foremost 3D printing techniques, *viz.*, stereolithography (SLA) and selective laser sintering (SLS), several other methods have been introduced such as material jetting, binder jetting, sheet lamination, and directed energy deposition (Deckers et al., 2014; Sames et al., 2016). Metal-based AM draws special attention due to the complex solidification behaviors and resultant microstructures that evolve during the fabrication. Despite these challenges, laser based AM has proven to be adaptable for the fabrication of various alloy parts (Frazier, 2014; Bandyopadhyay and Traxel, 2018; Moorehead et al., 2020; Sreeramagiri et al., 2020b). The ability of metal AM to manufacture components with intricate geometries, eliminates the need for tools and dyes, particularly for prototyping (Sreeramagiri et al., 2020a). Metal AM spans across a wide range of applications from energy, defense, transportation to healthcare (Dinda et al., 2008; Sreeramagiri et al., 2020b, 2020a).

Broadly metal AM can be categorized into *1*) powder bed fusion (PBF) and *2*) directed energy deposition (DED), as illustrated in **Figure 2**. PBF operates by spreading a thin layer of metal powder on the substrate followed by heat source (laser or electron beam) that selectively melts and solidifies the powder. In contrast, DED directs a focused heat source (laser/electron beam/metal arc) at a specified coordinate on the substrate to create a melt pool followed by depositing the feedstock (powder/wire) therein to create a clad of the material (Sreeramagiri et al., 2020a). Since a melt pool is created prior to the deposition of the feedstock, the constraints on the build rate due to the feed

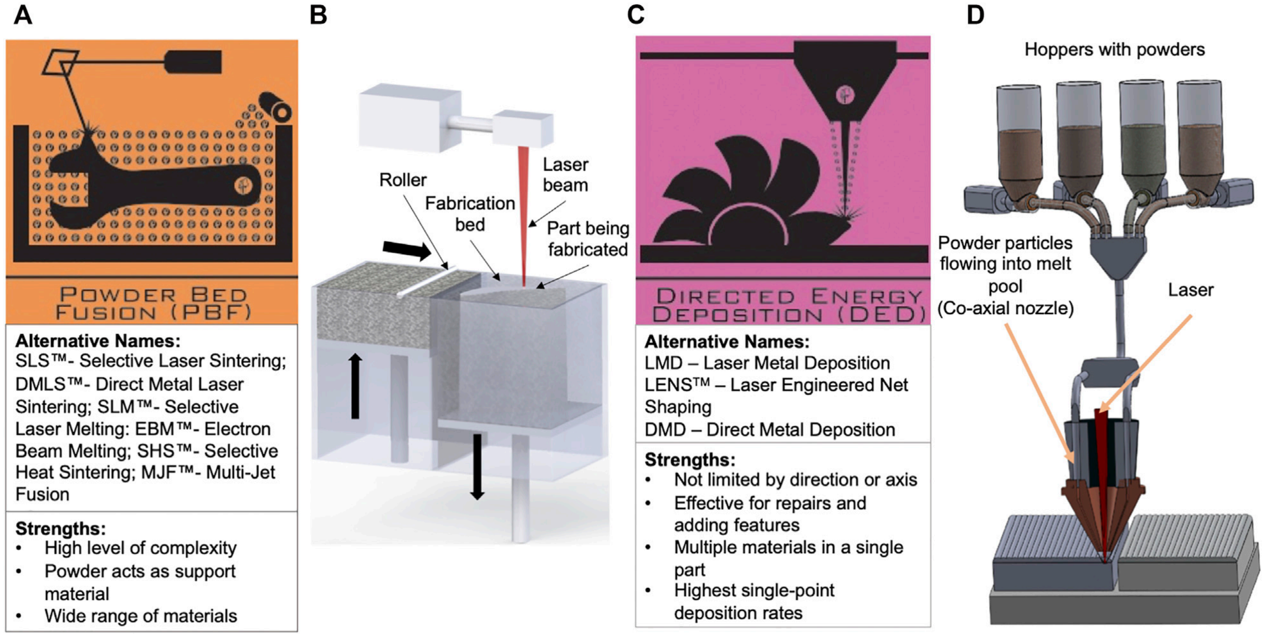

FIGURE 2 | (A,C) An overview of metal additive manufacturing processes according to ASTM (adopted from Hybrid Manufacturing Technologies) (Hybridmanutech, 2020); **(B)** Schematic of the powder bed fusion process illustrates a roller laying powder on the bed followed by a laser melting the cross section of part; **(D)** Schematic of direct energy (laser metal) deposition displays the laser melting a spot on the substrate while depositing the powder into the melt pool (Sreeramagiri et al., 2020b).

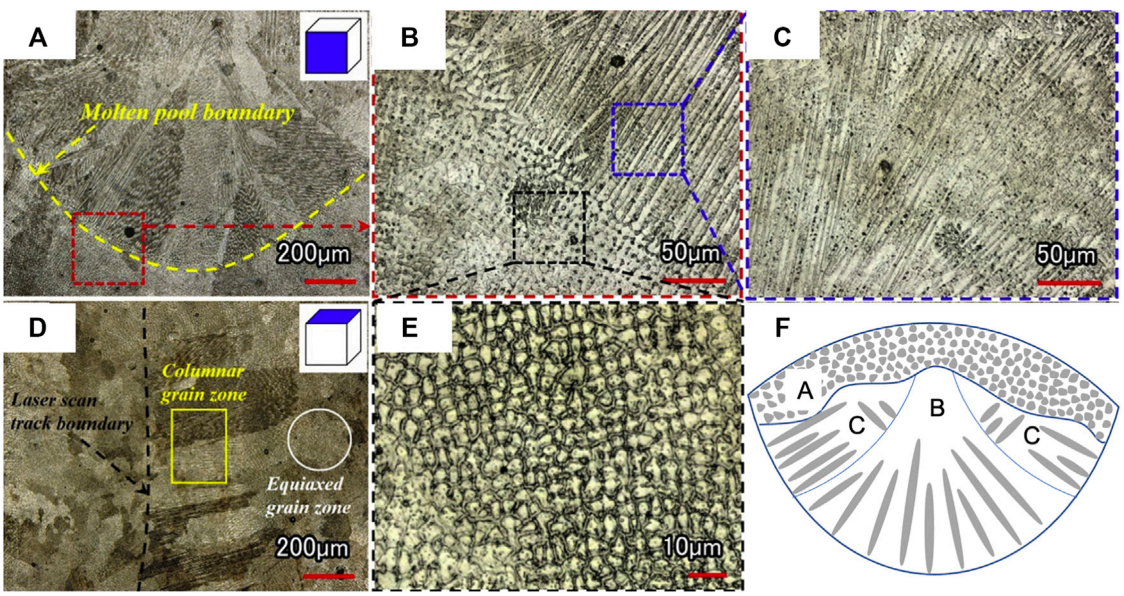

FIGURE 3 | A microstructural evolution during LMD of CoCrFeMnNi MPEA. **(A)** The microstructural characterization of clad near the melt-pool boundary; **(B)** A magnified representation of the melt pool boundary with equiaxed and columnar grains near the solid-liquid interface; **(C)** A magnified view of the epitaxially guided columnar growth from the solid-liquid interface; **(D)** A top view of the laser scan track; **(E)** A magnified display of **(B)** reveals the formation of equiaxed grains at the solid-liquid interface due to the concentrated energy source at the start; **(F)** A schematic representation of region "A" equiaxed grains in the melt-pool region surrounded by atmosphere, region "C" being the location of the melt-pool, with the peak intensity of the laser guided by a gaussian function, and region "B" is the overlap region where the melt-pool boundary facilitates a heterogenous nucleation point for columnar grains (Adopted from (Tong et al., 2019)).

TABLE 1 | Processing parameters and their associated energy densities for various additively manufactured MPEAs.

Alloy family	Phases exhibited	Heat treating temperatures	Process parameters: Laser power (W)	Beam diameter (mm)	Scan speed (mm/min)	Layer thickness (mm)	Energy density (J/mm^3)	Cracks Yes/No	Ref
$Co_{0.5}CrCu_{0.5}FeNi_{1.5}AlTi_{0.4}$	BCC+L21+Cu-rich Precipitates	—	—	—	—	—	—	No	Choudhuri et al. (2015)
AlCoCrCuFeNi	BCC	—	2,592	1	120	0.35	3,702.84	No	Yue et al. (2014)
AlCoCrFeNi	BCC+B2	N/A	500	0.2	150	0.15	6666.65	No	Kunce et al. (2015)
			500	0.2	1800	0.15	555.55	No	
			500	0.2	2,400	0.15	416.66	Yes	
Remelted x = 0.7	FCC + BCC		300	1.2	300	0.65	76.92	No	Ocelík et al. (2016)
Remelted x = 0.8	FCC + BCC		450	1.2	600	0.65	57.69	No	
Remelted x = 1	BCC		300	1.2	300	0.65	76.92	No	
As-deposited	BCC		600	2.3	300	0.75	69.56	No	
Direct Deposition	—		550	2	—	1	—	Yes	Cui et al. (2019)
Deposition with intermediate layer			550	2	—	1	—	No	
	B2/BCC	600°C – BCC	800	3	800	0.25	79.99	No	Wang et al. (2017)
		800°C – BCC + FCC + σ	800	3	800	0.25	79.99	—	
		1000°C – BCC + FCC	800	3	800	0.25	79.99	—	
		1200°C – BCC + FCC	800	3	800	0.25	79.99	—	
AlCoCrFeNi + YPSZ	Composite	N/A	1,000 3,000	—	240 1,200	—	—	Yes/No	Li et al. (2017)
$Al_xCoCrFeNi$ x = 0.3	FCC	N/A	800	4	800	0.25	59.99	No	Joseph et al. (2015)
x = 0.6	FCC+BCC		800	4	800	0.25	59.99	No	
x = 0.85	BCC		800	4	800	0.25	59.99	No	
x = 0.3	FCC	1000°C	800	2	800	0.49	61.22	—	Chao et al. (2017)
x = 0.6	FCC+BCC	1000°C	1,000	2	800	0.49	76.53	—	
x = 0.85	BCC	1000°C	1,200	2	800	0.49	91.83	—	
$Al_xCoCrFeNi$ $x \leq 0.37$	FCC	N/A	150	—	760	—	—	No	Li et al. (2018)
$0.41 < x \leq 0.48$	FCC + BCC								
$0.52 \leq x \leq 1.06$	FCC + BCC/B2								
$x > 1.16$	BCC/B2								
$Al_{0.3}CoCrFeNi$	FCC	As-deposited	300	0.5	102	0.254	1,389.52	—	Nartu et al. (2020)
		500°C	300	0.5	102	0.254	1,389.52		
		620°C	300	0.5	102	0.254	1,389.52		
AlTaCrFeNi	Multiple Phases	N/A	600	2.3	300	0.75	69.56	No	Ocelík et al. (2016)
FeCrCoMnNi	FCC	—	370	1.2	800	0.35	66.07	Yes	Haase et al. (2017)
	FCC	500°C – FCC	—	—	—	—	—	—	Tong et al. (2019)

(Continued on following page)

TABLE 1 | (*Continued*) Processing parameters and their associated energy densities for various additively manufactured MPEAs.

Alloy family	Phases exhibited	Heat treating temperatures	Process parameters					Cracks	Ref
			Laser power	Beam diameter	Scan speed	Layer thickness	Energy density	Yes/No	
			W	mm	mm/min	mm	J/mm^3		
		700°C – FCC+BCC	600	2	800	0.8	28.12	yes	
		900°C – FCC+BCC	800	2	800	0.8	37.49	—	
		1100°C – FCC	1,000	2	800	0.8	46.87	—	
	FCC + BCC precipitates in Grain Boundaries	N/A	300	2	600	0.6	24.99	No	Gao and Lu, (2019)
	FCC		400	0.6	300	0.46	289.85	No	Guan et al. (2019)
	FCC		1,000	1.8	500	0.4	166.66	No	Xiangt al. (2019b)
			1,200	1.8	500	0.4	199.99	No	
			1,400	1.8	500	0.4	233.33	No	

material can be circumvented by employing relatively high layer heights as a function of the beam diameter (b_d). Laser based metal DED, often referred to as laser metal deposition (LMD), offers several advantages such as combinatorial and functionally graded part fabrication, multicomponent alloy sub-elements for devices, and surface engineering by cladding (Sreeramagiri et al., 2020a; 2020b).

Most of the metal AM processes employ rapid melting and solidification of a metal/alloy powder to complete the part layer by layer. These melting-solidification cycles exert cooling rates ranging between 10^3–10^6 K/s (Li and Wang, 2010; Sreeramagiri et al., 2020a), crafting certain artifacts affecting the grain growth (**Figure 3**). For instance, **Figure 3A** represents one such artifact; the melt pool boundary, which results from a Gaussian laser power distribution. Tracing this boundary into the melt, reveals an epitaxially guided columnar growth in a direction opposite to the heat transfer (**Figure 3B**); however, the origins of columnar growth are equiaxed grains near the lower end of the boundary and indicative of a lower temperature gradient near the melt pool boundary (**Figure 3E**) (Tong et al., 2019; Sreeramagiri et al., 2020a).

The grain growth mechanism within the melt pool can be correlated with the interaction of laser with the HEA. The initial high intensity of laser beam promotes a low thermal gradient at the pool boundary when processing a bulk alloy sample, which consequently promotes an equiaxed growth followed by epitaxially guided columnar grains (Tong et al., 2019). As a result, the melt assumes highly textured microstructures (Joseph et al., 2015) and lattice strains (Sreeramagiri et al., 2021), which contribute to strengthening in the alloy (Roy et al., 2021b) and may occasionally be detrimental for printability (Ramakrishnan and Dinda, 2019; Sreeramagiri et al., 2020a).

MICROSTRUCTURES AND PROPERTIES OF MPEAS PROCESSED THROUGH DED

Certain MPEAs have been synthesized and subsequently characterized using the DED process (Chen et al., 2018; Li W. et al., 2018, 2019; Gorsse et al., 2018; George et al., 2019; Ostovari Moghaddam et al., 2021). Given the expansive compositional palette, we classify and analyze the findings for transition-metal based and refractory MPEAs, to collate the insights gained and the prospective for continued efforts.

The Cantor (CoCrFeMnNi) Family of MPEAs

The stable single phase of CoCrFeMnNi accompanied by its ductility makes it a good candidate material for laser metal deposition (LMD) to produce crack free, fully dense deposits (Choudhuri et al., 2015; Haase et al., 2017; Li R. et al., 2017; Wang et al., 2017, 2021; Qiu et al., 2018; Yao et al., 2018; Chew et al., 2019a; Gao and Lu, 2019; Guan et al., 2019; Tong et al., 2019; Xiang et al., 2019b, 2019a). However, insufficient energy densities during deposition can lead to cracks. **Tables 1**, **2** list the processing parameters employed for various alloys and their associated mechanical properties. Tong et al. (Tong et al., 2019) reported a marked of difference of ±20% ductility when

TABLE 2 | Mechanical properties of various additively manufactured MPEAs presented in **Table 1**.

Alloy system	Phases exhibited	Energy density	Mechanical properties data if available			Ref
	As-deposited	J/mm^3	Yield strength	Ultimate tensile strength	Ductility	
$Al_{0.3}CoCrFeNi$	FCC	59.99	200 MPa (True Stress)	—	1.0 (true Strain)	Joseph et al. (2015)
$Al_{0.6}CoCrFeNi$	FCC+BCC		400 MPa (True Stress)	—	0.5	
$Al_{0.85}CoCrFeNi$	BCC		1,400 MPa (True Stress)	—	0.25	
AlCoCrFeNi	B2/BCC	79.99	1.15 ± 0.15 GPa (Compressive true)	2.8 ± 0.2 GPa (Compressive true)	21.6 ± 4% (Compressive true)	Wang et al. (2017)
$Al_{0.3}CoCrFeNi$	FCC	1,389.52	410 MPa	500 ± 10 MPa	27%	Nartu et al. (2020)
	—		500 MPa	600 MPa	28%	
	FCC + $L1_2$		630 MPa	750 MPa	18%	
FeCrCoMnNi	FCC	66.07	260 MPa (compressive true)	—	52% (compressive true)	Haase et al. (2017)
	FCC	28.12–46.87	330 ± 30 MPa	530 ± 30 MPa	50 ± 20%	Tong et al. (2019)
	FCC + BCC precipitates in Grain Boundaries	24.99	460 MPa	620 MPa	57%	Gao and Lu, (2019)
	FCC	289.85	517 MPa	600 ± 20 MPa	17%	Guan et al. (2019)
	FCC	166.66	189	400 ± 20 MPa	40 ± 20%	Xiang et al. (2019b)
		199.99	—	500 ± 20 MPa	40 ± 15%	
		233.33	290 MPa	550 ± 5 MPa	50 ± 5%	

the process parameters are modified to tailor the microstructures and consequently the mechanical properties. Microstructures of the tensile test samples under the influence of three different laser powers revealed cracks initiated from pores of the sample processed at 28.12 J/mm^3. In contrast, the increased ductility of other samples, while retaining their strength, is conjectured as a consequence of reduced porosity that hinders the crack propagation, and the formation of fine grains resulting from high cooling rates (Chew et al., 2019b; Guan et al., 2019). Moreover, AM based fabrication is known to induce residual thermal stress of ~180 MPa (Guan et al., 2019). The thermal stress imparts an increased dislocation density in the component that subsequently renders plastic deformation (Sreeramagiri et al., 2021). Heat-treatment relieves these stresses, in turn enhancing the ductility of the alloy (Tong et al., 2019; Xiang et al., 2019b; Guan et al., 2019).

CoCrFeMnNi alloy predominantly favors a single-phase FCC solid solution (**Figure 4A**), with an infinitesimal fraction of Cr and Mn rich precipitates within the grains (**Figure 4C**). In contrast to the strengthening precipitates, Cr and Mn-rich precipitates act as the crack initiation sites and are considered detrimental to the mechanical properties (He et al., 2014; Qiu et al., 2018). Formation of these precipitates is attributed to the presence of Mn in composition and are eliminated in its absence (Gali and George, 2013). Besides precipitation, a homogenous distribution of candidate elements is realized in the alloy as evinced in **Figure 4D**. In addition to the precipitates within the grains, Gao et al. (Gao and Lu, 2019) reported the precipitation of BCC phase within the grain boundaries. The secondary BCC phase is attributed to the grain boundary wetting phase transformations (López et al., 2004; Straumal et al., 2008, 2012). An incomplete grain boundary wetting and the energies associated with the interfaces lead to the formation of a different phase along the grain boundaries.

Transition Metal MPEAs With Al Addition

Inclusion of Al in transition metal based MPEAs, essentially variations of Co-Cr-Fe-Ni composition, demonstrates a pronounced effect on the crystallographic phase by promoting a greater lattice misfit (Ma et al., 2017), valence electron configurations (Guo et al., 2011) and atomic packing efficiencies (Wang et al., 2009). These effects contribute to improving the MPEA's thermal stability (Ocelík et al., 2016) as well as their mechanical, electrical and magnetic properties (Chou et al., 2009; Borkar et al., 2016). A gamut of FCC and BCC structures are realized from LMD processing of $Al_xCoCrFeNi$ MPEAs as a function of Al content ($0 < x \le 2$) (Joseph et al., 2015, 2017; Kunce et al., 2015; Sistla et al., 2015; Ocelík et al., 2016; Borkar et al., 2016; Wang et al., 2017; Chao et al., 2017; Choudhuri et al., 2017; Ma et al., 2017; Li et al., 2018; Nartu et al., 2020). Specifically, $x = 0.15–0.37$ promotes an FCC phase, followed by a BCC/B2 precipitation in FCC at $x = 0.41$. Further increase in Al results in BCC/B2 domination at $x = 0.69$ with the initiation of FCC precipitation at the grain boundaries (~3.6% FCC phase fraction from XRD and EBSD). The alloy exhibits a single phase BCC/B2 at $x = 1.16$ (Joseph et al., 2015; Li et al., 2018).

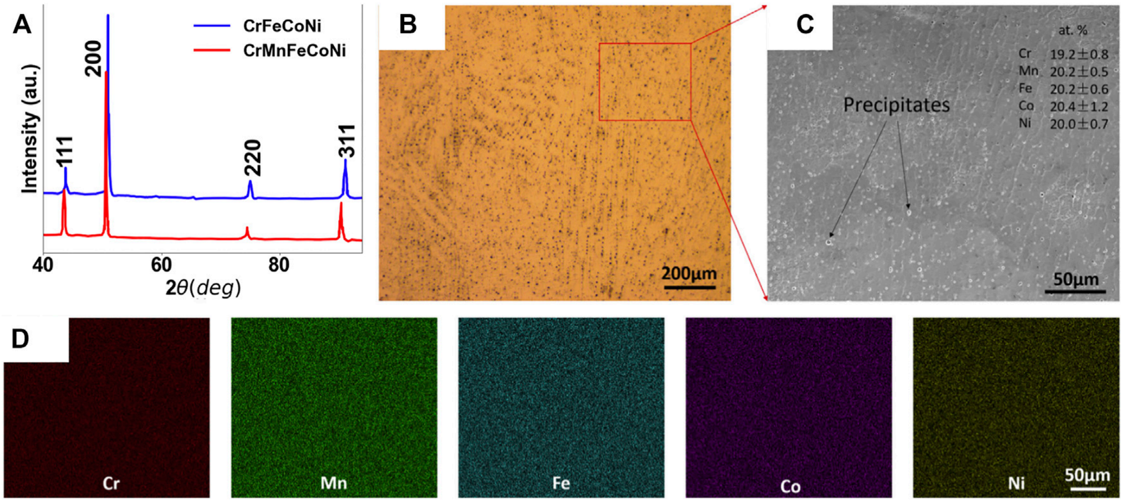

FIGURE 4 | (A) XRD plots of CrFeCoNi and CrMnFeCoNi HEAs represents the formation of a single-phase solid solution (Wang et al., 2021), **(B)** Optical micrograph of CrFeCoNiMn HEA with a typical dendritic structure, **(C)** SEM image of CrFeCoNiMn reveals the presence of Cr and Mn-rich precipitates in the grains, **(D)** EDS map reveals a homogenous composition distribution of candidate elements in the alloy (Qiu et al., 2018).

Figure 5 displays the microstructural evolution of $Al_xCoCrFeNi$ MPEA, with the XRD (**Figure 5A**) suggesting the formation of single-phase solid solutions. As presented in **Figure 5B**, a minimal addition of Al in the alloy (x = 0.3) can lead to segregation (of Al) in the grain boundaries, while maintaining a homogenous distribution within the grain. Although the XRD advocates the realization of single-phase solid solutions, scrutinizing the microstructures at various compositions reveals the formation of secondary precipitates. Examining the EDS maps within the precipitates, corroborate the formation of Al-Ni rich B2 precipitates in the BCC matrix alongside FCC when x = 0.6 (**Figure 5C**). Further increase in Al (beyond x = 0.8) promotes the domination of BCC while inverting the matrix and precipitates to form an ordered B2 matrix with disordered BCC precipitates (**Figure 5D**). These transformations in the crystal structure cause a significant increase in the hardness of material, while maintaining the elastic modulus, as illustrated in **Figure 6** (Kunce et al., 2015; Nartu et al., 2020).

In addition to hardness, certain fractions of Al in the MPEA (0.3 ≤ x ≤ 0.6) modify the grain microstructure from columnar to equiaxed due to an enhanced thermal conductivity with increasing Al concentration (Kukshal et al., 2018). Nonetheless, continued increase in Al reverts back the MPEA grains to columnar structures due to the phonon scattering across the dual phase boundary (Joseph et al., 2015). Heat treating the as-deposited samples at 1200°C improves the compressive strength and corrosive resistance of the alloy (Wang et al., 2017). Besides heat-treatment, hot isostatic pressing can potentially enhance structural properties of MPEAs, though σ phase precipitation is reported during the processing (Joseph et al., 2018).

The presence of steep thermal gradients during the processing promotes the formation of columnar grains with preferred orientations. Occasionally, these grain alignments result in asymmetric tensile and compressive properties due to the formation of deformation twins (Wang et al., 2017; Joseph et al., 2017). Again, the high hardness of AlCoCrFeNi is occasionally insufficient to achieve the targeted wear resistance; this limitation is often circumvented by adding yttria (partially) stabilized ZrO_2 (YPSZ) to AlCoCrFeNi (Li et al., 2017). The suspended YPSZ particles serve as the primary heterogenous nucleation sites and support the growth of finer grains that enhance the mechanical properties such as wear resistance, although occurrence of cracks in the deposited samples requires deeper scrutiny.

The complex melt pool dynamics coupled with the dilution of the alloy on the substrate during LMD necessitates the substrate composition to be compatible with the clad material to eliminate the formation and propagation of cracks. For instance, deposition of AlCoCrFeNi on AISI 304 leads to cracks at the interface due to incompatible thermal expansion coefficients (α_L) (Cui et al., 2019), while a SS316L substrate with $\alpha_L = 9 \times 10^{-6}$/K close to that of AlCoCrFeNi (9–13 × 10^{-6}/K (Chou et al., 2009)) produces crack free deposits. Irrespective of the choice of substrates, selection of improper processing parameters can lead to the formation of cracks during deposition. In addition to electrical and mechanical properties, $Al_xCoCrFeNi$ family of MPEAs also exhibit novel magnetic properties. A variation in x from *0* to *1.3* increases the saturation magnetization in the MPEA, but the same decreases for $x > 1.3$ (Borkar et al., 2016). The trends in the magnetic properties are attributed to the phase stabilities of the alloys.

Evaporation of the principal elements due to the differences in boiling points constitutes another challenge for MPEA synthesis using LMD. When processing CoCrCuFeNiAl MPEA on a Mg substrate, Yue et al. (Yue et al., 2014) observed evaporation of Mg due to the excess thermal energy directed on the substrate to suitably melt all the alloying elements. Additionally, Cu diffused

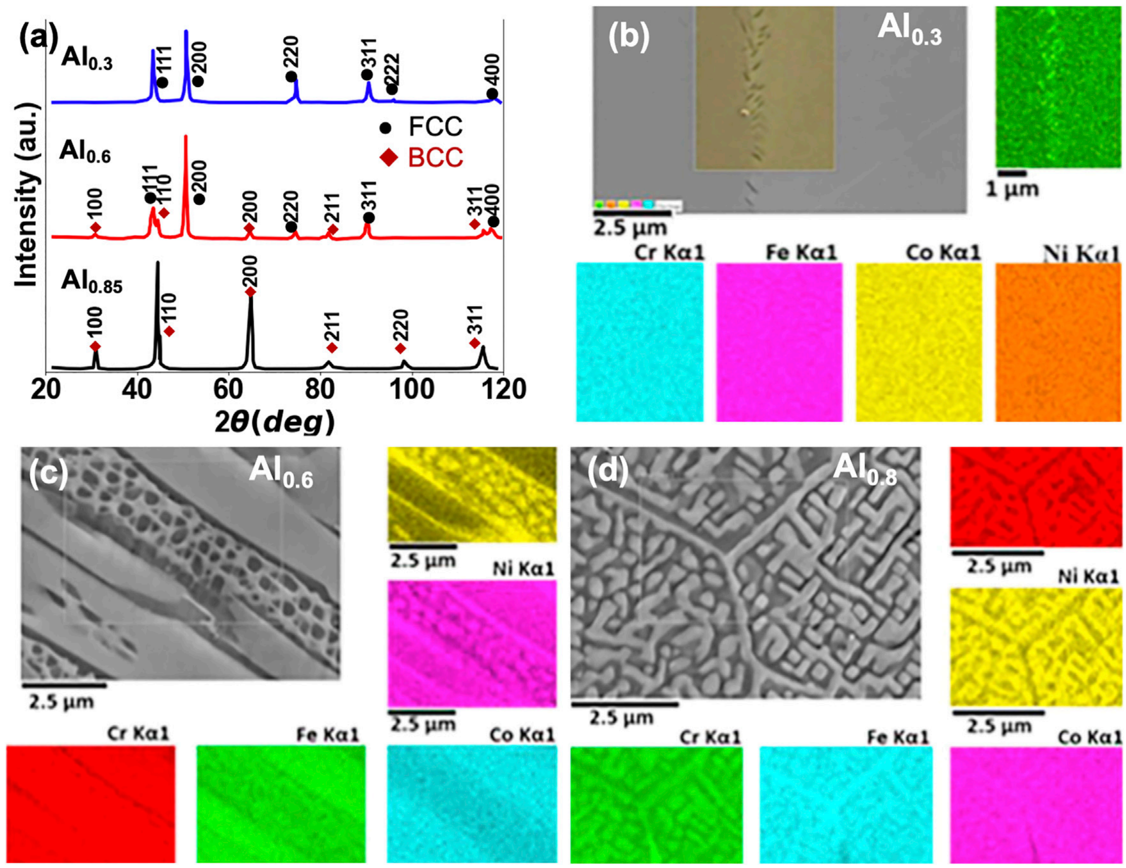

FIGURE 5 | Effect of Al content on the microstructural evolution of $Al_xCoCrFeNi$. **(A)** XRD plot reveals the realization of multiple phases under varying Al composition, **(B)** x = 0.3: single phase FCC solid solution with Al segregation along the grain boundaries and homogenous distribution of candidate elements in the alloy, **(C)** x = 0.6: duplex FCC+BCC/B2, reveals Cr-Fe rich BCC phase containing B2 Al-Ni rich precipitates, **(D)** x = 0.8: Single phase inverted microstructure, with Al-Ni rich B2 matrix and Cr-Fe rich BCC precipitates (adopted from (Joseph et al., 2015)).

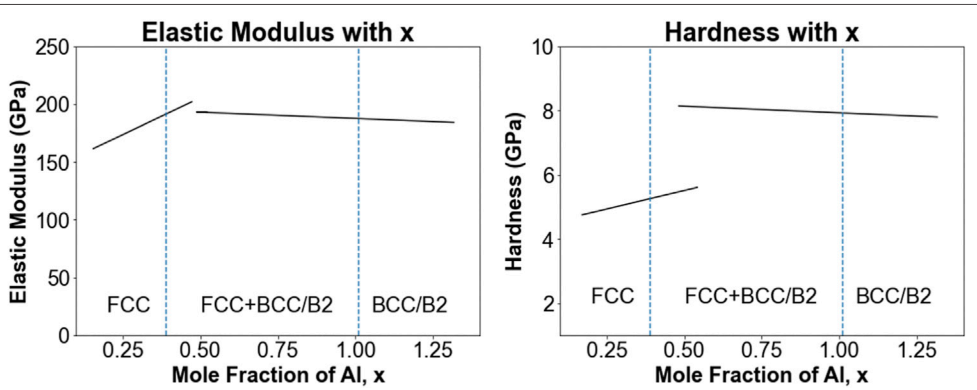

FIGURE 6 | Effect of Al content on the mechanical properties of AlxCoCrFeNi. **(A)** Increasing Al content does not have a significant effect on the elastic modulus, **(B)** Hardness of the alloy increases as the Al content is increased (adopted from Mu et al.). (adopted from (Li et al., 2018)).

into the Mg melt during the processing and the solidification mechanism followed the Mg-Cu phase diagram. The alloy exhibited a dual phase BCC/B2 crystal structure with a 1.5 nm coherent interfacial layer. The interfacial transition layer revealed a B2 crystallographic phase with a distinct sub-lattice occupancy resembling a $L2_1$ ordered Huesler-like compound (Welk et al.,

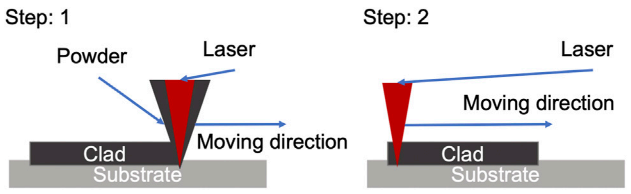

FIGURE 7 | A schematic illustration of the multi-step laser metal deposition. Step-1 represents the laser impinging on the substrate and depositing the powder in the melt pool. Step-2 illustrates the laser melting and solidifying the same track without powder to homogenize the deposited clad.

2013; Choudhuri et al., 2015). Likewise, during LMD of TiVCrAlSi equimolar MPEA using elemental powders on a Ti-6Al-4V substrate, evaporation of Al is recorded due to its low boiling point. These evaporation issues can be mitigated by calibrating the powder input as a function of the evaporation rates during the process parameter selection. The TiVCrAlSi MPEA produced a BCC matrix with $(Ti,V)_5Si_3$ ordered precipitates that in turn contributed to an enhanced wear resistance (Huang et al., 2012b).

Refractory MPEAs

DED synthesis of MPEAs composed of refractory elements is of significant interest due to the limitations on the mold temperatures for conventional processes like casting or powder metallurgy (Kunce et al., 2013; Kunce et al., 2014). On the other hand, LMD is accompanied by process induced artifacts such as pores and cracks, and their tendency to rapidly oxidize (Dobbelstein et al., 2016, 2018, 2019; Stawovy, 2018; Li et al., 2020b; Moorehead et al., 2020). The high melting points of the refractory metals mandate the utilization of a high laser power, while the rapid cooling intrinsic to the process creates high thermal stresses that contribute to the formation of cracks during the deposition. Techniques employing a single-track weld bead have proven challenging for the processing of MoNbTaW (Dobbelstein et al., 2016) and TiNbZrHfTa (Dobbelstein et al., 2018) MPEAs, whence cracks are formed in the deposit due to high thermal stresses. An approach to bypass the crack formation is through pre-heating of the substrates (Li et al., 2020b). Pre-heating the substrate to 500°C promotes a brittle to ductile transition in certain elements such as W (Li B.-S. et al., 2020), which can inhibit cracks in the deposit (Dobbelstein et al., 2016; Li et al., 2020b). A modification to the LMD by employing multi-step deposition can potentially prevent the genesis of cracks. As illustrated in **Figure 7**, multi-step LMD involves one pass for deposition (depositing and melting the powder) and a few additional passes, termed as “re-melting,” along the same line without the feed material by a defocused the laser beam. This approach has proven favorable to achieve homogenous dense depositions when processing refractory MPEAs (Dobbelstein et al., 2016).

It is important to note that the extensive differences in melting points and high laser powers cause insufficiently melt elements, poor fusion of the alloy, and in select cases, the evaporation of elemental powders. **Figure 8** illustrates the microstructures from the deposition with a single laser pass that fails to melt a certain fraction of the powder particles (as evinced through EDS) due to the induced energy being inadequate for the fusion. However, remelting the deposited track without powder ensures sufficient power to melt all the powder particles, realizing a homogenous compositional distribution as shown in **Figure 8B**. Evaporation is an even greater concern during *in-situ* alloying when a wide temperature difference exists in the melting points of the constituent principal elements. Powder calibration and use of pulsed laser source to deposit the alloy is deemed as a potential solution to overcome this drawback (Moorehead et al., 2020). Deposition of Mo, Nb, Ta, W libraries using this technique enables the evaluation of several compositions, which assume a single-phase disordered BCC solid-solution (analyzed through XRD). The BCC in these alloys is stabilized by the addition of Nb, while B2 precipitates form with an increase in concentration of Ta, as shown in **Figure 9**. Characterization of one of these libraries demonstrates a homogenous candidate distribution with relatively small grains (compared to arc-melting) as presented in **Figure 10**. Scrutinizing the microstructures, suggests the domination of grains by W and Ta, with the grain boundaries populated with Mo and Nb. This mode of segregation is attributed to the difference in solubility of elements in liquid and solid phases (from a thermodynamic standpoint) in conjunction with the effects of undercooling. Further homogenization of these alloys can be achieved by heat-treatment.

Processing of a medium entropy MoNbTa (BCC) alloy by DED revealed a significant improvement in ductility at the cost of yield strength relative to arc-melted samples (Li et al., 2020b). The reduction in yield strength is attributed to the metallurgical defects such as cracks during the fabrication by LMD, although a fundamental mechanism to explain the increase in the ductility with the presence of cracks in the deposit is warranted. The lack of data on the AM of MPEAs offer inconclusive evidence for such observations, but provide the motivation for continued efforts in this research domain.

OUTLOOK

The exploration and discovery of novel MPEA compositions has been accelerated by computational and data-enabled methods such as machine learning. Still, validation of these predictive MPEA compositions and subsequently the component fabrication using conventional techniques remains a challenge. AM can assist in high-throughput experiments by combinatorial synthesis of a large population of MPEAs from within a family of metals, transition to refractories and beyond. However, the complex solidification behavior due to the high cooling rates and differences in the melting points of the constituent elements often induce unanticipated artifacts in the microstructures. Specifically, the steep thermal gradients and the rapid cooling foster directional solidification, epitaxial growth, and highly textured microstructures in the alloys. On one hand, MPEAs can benefit from these material features, especially fine-grained

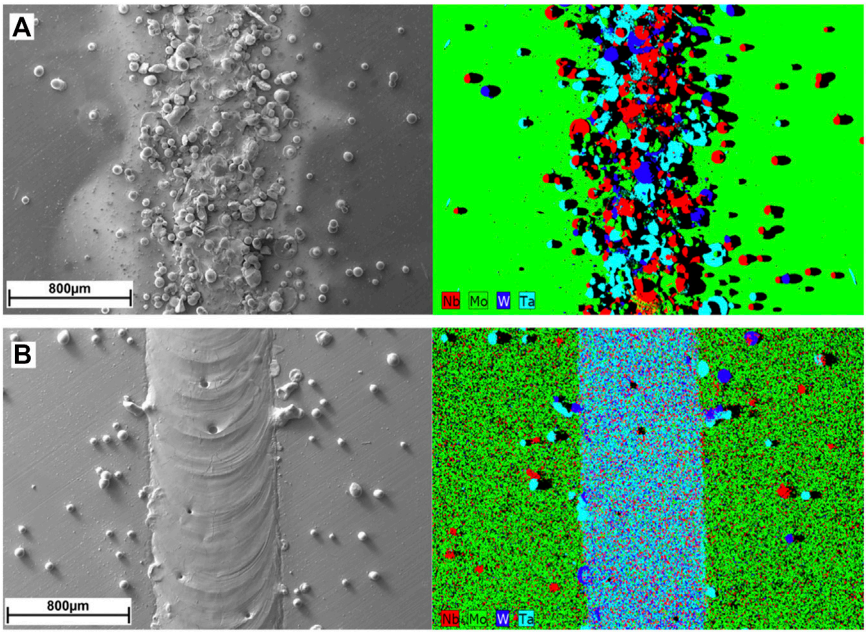

FIGURE 8 | LMD of MoNbTaW refractory MPEA. **(A)** Representation of the initial deposition track of the MPEA. Unmelted powder particles can be seen all over the track due to lack of sufficient power during deposition. **(B)** Remelted track of the MPEA. A clear, mixed and a homogenous track can be seen after remelting the initially deposited track. Remelting was done with significantly higher power that can suitably melt most of the particles (Dobbelstein et al., 2016).

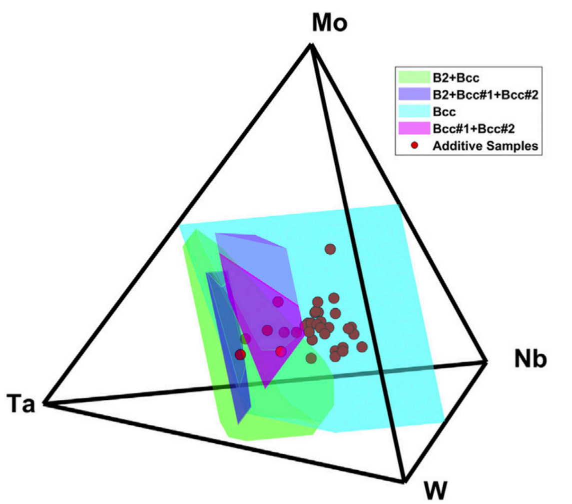

FIGURE 9 | Quaternary phase diagram of MoNbTaW family of refractory MPEAs. The illustration highlights the stable phases at 300°C spanning the numerous possible compositions of this family (Moorehead et al., 2020).

microstructures, and possess superior mechanical properties relative to those synthesized by conventional subtractive manufacturing techniques. On the other hand, microstructural phase evolution in these alloys during DED, can also be detrimental when mismatch in substrate and MPEA lattice and thermal properties is evinced, and can lead to the formation of cracks as a function of composition. For instance, the transition metal based CoCrFeNiMn MPEA when alloyed with Al exhibits an increased lattice misfit, resulting in relatively higher hardness, but with cracks due to incompatible substrate and/or process parameters. Hence, defects arise primarily due to the substrate-material incompatibility. On the other hand, refractory MPEAs are naturally hard due to their crystallographic phase and assume cracks due to the lack of sufficient energy densities ($E = \frac{P}{v.b_d.t}$, where; P-laser power, v-scan speed (m/s), b_d-beam diameter (mm) and t-layer thickness (mm)). Here, defects are a consequence of improper processing parameters employed, potentially due to poor weldability (as a function of the composition) of the alloy. Thus, an intelligent selection of substrate material and temperature, process parameters and modified multi-step deposition approach, as discussed above, can eliminate such artifacts related to DED fabrication of functional MPEA components, albeit at an increased cost.

In the context of high-throughput synthesis for alloy development, candidate compositions (within a family of alloys) which do not crack while deposition (using a wide range of process parameters) are deemed to be easily printable with modest and quick process optimization strategies. Process optimization for these candidates is directed towards minimizing process induced porosities and applies to a set of compositions, thus enabling rapid screening of alloys with a single set of process parameters (Sreeramagiri et al., 2020b). On the contrary, compositions with inherent cracks realized during deposition are deemed hard to process and need further optimization techniques, which may be resource expensive (specifically for refractory MPEAs). Nevertheless, post alloy discovery, the conundrum of optimizing process parameters for difficult to

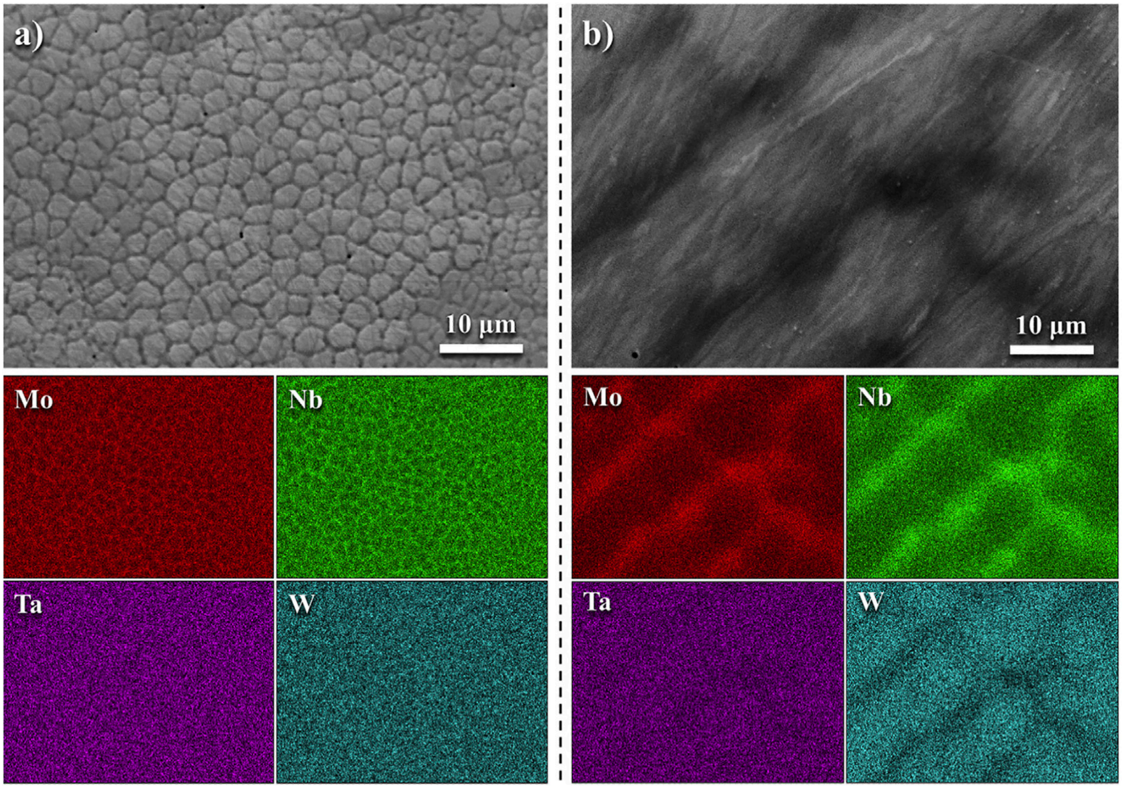

FIGURE 10 | A comparison of grain sizes and distributions in samples processed *via* additive manufacturing and arc-melting, **(A)** AMed sample reveals the formation of small grains due to the undercooling effects, **(B)** relatively larger grains in arc-melted samples. Both the processes reveal a near homogenous composition distribution with W and Ta within the grains, while the Mo and Nb segregated at the boundaries (adopted from (Moorehead et al., 2020)).

synthesize alloy compositions versus resorting to fabricable materials with a compromise on mechanical properties is application-specific and requires deeper scrutiny. This challenge relates to emerging research efforts geared towards establishing relations between composition-substrate compatibility as well as process parameter selection and printability, to tailor compositions and microstructures for targeted properties.

For the processing of refractory MPEAs, the high melting temperatures of the principal elements dictate the application of excessive laser power and energy density. Such high temperature processing, increases the possibility of oxidation of the constituent metals, necessitating the need to include elements in the MPEA composition that can form passivating (and possibly complex) stable oxides on the sample surface. Moreover, the density of the MPEA and the compositional defects such as porosity are also dependent on the employed process parameters. Hence, an effective approach to overcome these defects for reproducible and robust LMD of MPEAs will be to implement data-informed optimal processing parameters (P, v, t, etc.) to achieve fully dense deposits (de Oliveira et al., 2005; Shen et al., 2015; Bandyopadhyay and Traxel, 2018; Debroy et al., 2018; Michopoulos et al., 2018; Johnson et al., 2019; Scime and Beuth, 2019; Sreeramagiri et al., 2020a, 2020b; Deneault et al., 2021; Zhang et al., 2021). A thorough understanding of the physical and microstructural effects that DED processing parameters inflicts on various properties of the alloy (*viz.*, mechanical, chemical, electrical, etc.) is of paramount importance (**Figure 11**). These process-structure-property relations in conjunction with

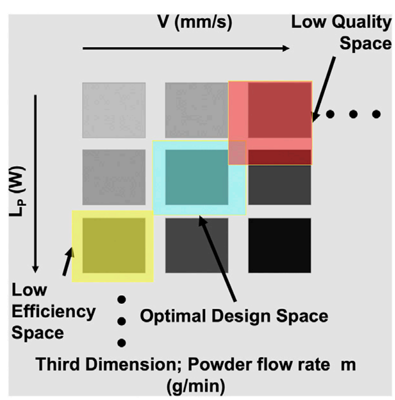

FIGURE 11 | A 3D landscape for the design of experiments (DoE) comprising the laser power (L_P), scan speed (V) and the powder flow rate (m). A high laser power with a low velocity is inefficient, while a high velocity with a low laser power is detrimental to the deposit quality. Therefore, a tradeoff between these parameters is important to achieve high quality deposits.

conventional design of experiments will aid in an efficient choice of process parameters leading to fully dense, defect-free and stable deposits.

AUTHOR CONTRIBUTIONS

PS: Formal analysis, Investigation, Methodology, Visualization, Writing - original draft, Writing - review & editing. GB: Conceptualization, Funding acquisition, Project administration, Resources, Supervision, Writing - original draft, Writing - review & editing.

FUNDING

The research was supported by the National Science Foundation (NSF) through the award # CMMI-1944040. Any opinions, findings, conclusions, or recommendations expressed in this material are those of the authors' and do not necessarily reflect the views of the NSF.

REFERENCES

Andersson, J.-O., Helander, T., Höglund, L., Shi, P., and Sundman, B. (2002). Thermo-Calc & DICTRA, Computational Tools for Materials Science. *Calphad* 26, 273–312. doi:10.1016/s0364-5916(02)00037-8

Antillon, E., Woodward, C., Rao, S. I., Akdim, B., and Parthasarathy, T. A. (2020). Chemical Short Range Order Strengthening in a Model FCC High Entropy alloy. *Acta Materialia* 190, 29–42. doi:10.1016/j.actamat.2020.02.041

Bandyopadhyay, A., and Traxel, K. D. (2018). Invited Review Article: Metal-Additive Manufacturing-Modeling Strategies for Application-Optimized Designs. *Additive Manufacturing* 22, 758–774. doi:10.1016/j.addma.2018.06.024

Borkar, T., Gwalani, B., Choudhuri, D., Mikler, C. V., Yannetta, C. J., Chen, X., et al. (2016). A Combinatorial Assessment of AlxCrCuFeNi2 (0. *Acta Materialia* 116, 63–76. doi:10.1016/j.actamat.2016.06.025

Cantor, B., Chang, I. T. H., Knight, P., and Vincent, A. J. B. (2004). Microstructural Development in Equiatomic Multicomponent Alloys. *Mater. Sci. Eng. A* 375-377, 213–218. doi:10.1016/j.msea.2003.10.257

Cantor, B. (2014). Multicomponent and High Entropy Alloys. *Entropy* 16, 4749–4768. doi:10.3390/e16094749

Chao, Q., Guo, T., Jarvis, T., Wu, X., Hodgson, P., and Fabijanic, D. (2017). Direct Laser Deposition Cladding of Al CoCrFeNi High Entropy Alloys on a High-Temperature Stainless Steel. *Surf. Coat. Technol.* 332, 440–451. doi:10.1016/j.surfcoat.2017.09.072

Chen, S., Tong, Y., and Liaw, P. (2018). Additive Manufacturing of High-Entropy Alloys: A Review. *Entropy* 20, 937. doi:10.3390/e20120937

Chew, Y., Bi, G. J., Zhu, Z. G., Ng, F. L., Weng, F., Liu, S. B., et al. (2019a). Microstructure and Enhanced Strength of Laser Aided Additive Manufactured CoCrFeNiMn High Entropy alloy. *Mater. Sci. Eng. A* 744, 137–144. doi:10.1016/j.msea.2018.12.005

Chew, Y., Bi, G. J., Zhu, Z. G., Ng, F. L., Weng, F., Liu, S. B., et al. (2019b). Microstructure and Enhanced Strength of Laser Aided Additive Manufactured CoCrFeNiMn High Entropy alloy. *Mater. Sci. Eng. A* 744, 137–144. doi:10.1016/j.msea.2018.12.005

Chou, H.-P., Chang, Y.-S., Chen, S.-K., and Yeh, J.-W. (2009). Microstructure, Thermophysical and Electrical Properties in AlxCoCrFeNi ($0 \le x \le 2$) High-Entropy Alloys. *Mater. Sci. Eng. B* 163, 184–189. doi:10.1016/j.mseb.2009.05.024

Choudhuri, D., Alam, T., Borkar, T., Gwalani, B., Mantri, A. S., Srinivasan, S. G., et al. (2015). Formation of a Huesler-like L21 Phase in a CoCrCuFeNiAlTi High-Entropy alloy. *Scripta Materialia* 100, 36–39. doi:10.1016/j.scriptamat.2014.12.006

Choudhuri, D., Gwalani, B., Gorsse, S., Mikler, C. V., Ramanujan, R. V., Gibson, M. A., et al. (2017). Change in the Primary Solidification Phase from Fcc to Bcc -based B2 in High Entropy or Complex Concentrated Alloys. *Scripta Materialia* 127, 186–190. doi:10.1016/j.scriptamat.2016.09.023

Cui, W., Karnati, S., Zhang, X., Burns, E., and Liou, F. (2019). Fabrication of AlCoCrFeNi High-Entropy alloy Coating on an AISI 304 Substrate via a CoFe2Ni Intermediate Layer. *Entropy* 21, 2. doi:10.3390/e21010002

de Oliveira, U., Ocelík, V., and De Hosson, J. T. M. (2005). Analysis of Coaxial Laser Cladding Processing Conditions. *Surf. Coat. Technol.* 197, 127–136. doi:10.1016/j.surfcoat.2004.06.029

Debroy, T., Wei, H. L., Zuback, J. S., Mukherjee, T., Elmer, J. W., Milewski, J. O., et al. (2018). Additive Manufacturing of Metallic Components - Process, Structure and Properties. *Prog. Mater. Sci.* 92, 112–224. doi:10.1016/j.pmatsci.2017.10.001

Deckers, J., Vleugels, J., and Kruth, J.-P. (2014). Additive Manufacturing of Ceramics: A Review. *J. Ceram. Sci. Technol.* 5, 245–260. doi:10.4416/JCST2014-00032

Deneault, J. R., Chang, J., Myung, J., Hooper, D., Armstrong, A., Pitt, M., et al. (2021). Toward Autonomous Additive Manufacturing: Bayesian Optimization on a 3D Printer. *MRS Bull.* 46 (7), 566–575. doi:10.1557/S43577-021-00051-1

Dinda, G. P., Dasgupta, A. K., and Mazumder, J. (2009). Laser Aided Direct Metal Deposition of Inconel 625 Superalloy: Microstructural Evolution and thermal Stability. *Mater. Sci. Eng. A* 509, 98–104. doi:10.1016/j.msea.2009.01.009

Dinda, G. P., Song, L., and Mazumder, J. (2008). Fabrication of Ti-6Al-4V Scaffolds by Direct Metal Deposition. *Metall. Mat Trans. A.* 39, 2914–2922. doi:10.1007/s11661-008-9634-y

Ding, J., Asta, M., and Ritchie, R. O. (2018). Melts of CrCoNi-Based High-Entropy Alloys: Atomic Diffusion and Electronic/atomic Structure from Ab Initio Simulation. *Appl. Phys. Lett.* 113, 111902. doi:10.1063/1.5045216

Dobbelstein, H., Gurevich, E. L., George, E. P., Ostendorf, A., and Laplanche, G. (2018). Laser Metal Deposition of a Refractory TiZrNbHfTa High-Entropy alloy. *Additive Manufacturing* 24, 386–390. doi:10.1016/j.addma.2018.10.008

Dobbelstein, H., Gurevich, E. L., George, E. P., Ostendorf, A., and Laplanche, G. (2019). Laser Metal Deposition of Compositionally Graded TiZrNbTa Refractory High-Entropy Alloys Using Elemental Powder Blends. *Additive Manufacturing* 25, 252–262. doi:10.1016/j.addma.2018.10.042

Dobbelstein, H., Thiele, M., Gurevich, E. L., George, E. P., and Ostendorf, A. (2016). Direct Metal Deposition of Refractory High Entropy Alloy MoNbTaW. *Phys. Proced.* 83, 624–633. doi:10.1016/j.phpro.2016.08.065

Fernández-Caballero, A., Wróbel, J. S., Mummery, P. M., and Nguyen-Manh, D. (2017). Short-Range Order in High Entropy Alloys: Theoretical Formulation and Application to Mo-Nb-Ta-V-W System. *J. Phase Equilib. Diffus.* 38, 391–403. doi:10.1007/s11669-017-0582-3

Frazier, W. E. (2014). Metal Additive Manufacturing: A Review. *J. Materi Eng. Perform.* 23, 1917–1928. doi:10.1007/s11665-014-0958-z

Gali, A., and George, E. P. (2013). Tensile Properties of High- and Medium-Entropy Alloys. *Intermetallics* 39, 74–78. doi:10.1016/j.intermet.2013.03.018

Gao, M., and Alman, D. (2013). Searching for Next Single-phase High-Entropy Alloy Compositions. *Entropy* 15, 4504–4519. doi:10.3390/e15104504

Gao, X., and Lu, Y. (2019). Laser 3D Printing of CoCrFeMnNi High-Entropy alloy. *Mater. Lett.* 236, 77–80. doi:10.1016/j.matlet.2018.10.084

George, E. P., Raabe, D., and Ritchie, R. O. (2019). High-entropy Alloys. *Nat. Rev. Mater.* 4, 515–534. doi:10.1038/s41578-019-0121-4

Gianelle, M., Kundu, A., Anderson, K. P., Roy, A., Balasubramanian, G., and Chan, H. M. (2020). A Novel Ceramic Derived Processing Route for Multi-Principal Element Alloys. *Mater. Sci. Eng. A* 793, 139892. doi:10.1016/j.msea.2020.139892

Gibson, I., Rosen, D. W., and Stucker, B. (2014). *Additive Manufacturing Technologies*. Berlin, Germany: Springer.

Gludovatz, B., Hohenwarter, A., Thurston, K. V. S., Bei, H., Wu, Z., George, E. P., et al. (2016). Exceptional Damage-Tolerance of a Medium-Entropy alloy CrCoNi at Cryogenic Temperatures. *Nat. Commun.* 7, 10602. doi:10.1038/ncomms10602

Gorsse, S., Couzinié, J.-P., and Miracle, D. B. (2018). From High-Entropy Alloys to Complex Concentrated Alloys. *Comptes Rendus Physique* 19, 721–736. doi:10.1016/j.crhy.2018.09.004

Guan, S., Wan, D., Solberg, K., Berto, F., Welo, T., Yue, T. M., et al. (2019). Additive Manufacturing of fine-grained and Dislocation-Populated CrMnFeCoNi High Entropy alloy by Laser Engineered Net Shaping. *Mater. Sci. Eng. A* 761, 138056. doi:10.1016/j.msea.2019.138056

Guo, S., Ng, C., Lu, J., and Liu, C. T. (2011). Effect of Valence Electron Concentration on Stability of Fcc or Bcc Phase in High Entropy Alloys. *J. Appl. Phys.* 109, 103505. doi:10.1063/1.3587228

Haase, C., Tang, F., Wilms, M. B., Weisheit, A., and Hallstedt, B. (2017). Combining Thermodynamic Modeling and 3D Printing of Elemental Powder Blends for High-Throughput Investigation of High-Entropy Alloys - towards Rapid alloy Screening and Design. *Mater. Sci. Eng. A* 688, 180–189. doi:10.1016/j.msea.2017.01.099

He, J. Y., Zhu, C., Zhou, D. Q., Liu, W. H., Nieh, T. G., and Lu, Z. P. (2014). Steady State Flow of the FeCoNiCrMn High Entropy alloy at Elevated Temperatures. *Intermetallics* 55, 9–14. doi:10.1016/J.INTERMET.2014.06.015

Huang, C., Zhang, Y., Vilar, R., and Shen, J. (2012a). Dry Sliding Wear Behavior of Laser Clad TiVCrAlSi High Entropy alloy Coatings on Ti-6Al-4V Substrate. *Mater. Des.* 41, 338–343. doi:10.1016/j.matdes.2012.04.049

Huang, C., Zhang, Y., Vilar, R., and Shen, J. (2012b). Dry Sliding Wear Behavior of Laser Clad TiVCrAlSi High Entropy alloy Coatings on Ti-6Al-4V Substrate. *Mater. Des.* 41, 338–343. doi:10.1016/j.matdes.2012.04.049

Hybridmanutech (2020). Quick Reference:7 Families of Additive Manufacturing. Available at: http://www.hybridmanutech.com/uploads/2/3/6/9/23690678/7_families_of_3d_printing_by_hybrid_v11_2p.pdf.

Jia, Q., and Gu, D. (2014). Selective Laser Melting Additive Manufacturing of Inconel 718 Superalloy Parts: Densification, Microstructure and Properties. *J. Alloys Compd.* 585, 713–721. doi:10.1016/j.jallcom.2013.09.171

Johnson, D., Singh, R., Singh, P., Sharma, A., and Balasubramanian, G. (2020). Accelerating the Computational Design of Multi-Principle Element Alloys. *Bull. Am. Phys. Soc.* 65, 1.

Johnson, L., Mahmoudi, M., Zhang, B., Seede, R., Huang, X., Maier, J. T., et al. (2019). Assessing Printability Maps in Additive Manufacturing of Metal Alloys. *Acta Materialia* 176, 199–210. doi:10.1016/J.ACTAMAT.2019.07.005

Joseph, J., Hodgson, P., Jarvis, T., Wu, X., Stanford, N., and Fabijanic, D. M. (2018). Effect of Hot Isostatic Pressing on the Microstructure and Mechanical Properties of Additive Manufactured AlxCoCrFeNi High Entropy Alloys. *Mater. Sci. Eng. A* 733, 59–70. doi:10.1016/j.msea.2018.07.036

Joseph, J., Jarvis, T., Wu, X., Stanford, N., Hodgson, P., and Fabijanic, D. M. (2015). Comparative Study of the Microstructures and Mechanical Properties of Direct Laser Fabricated and Arc-Melted Al X CoCrFeNi High Entropy Alloys. *Mater. Sci. Eng. A* 633, 184–193. doi:10.1016/j.msea.2015.02.072

Joseph, J., Stanford, N., Hodgson, P., and Fabijanic, D. M. (2017). Tension/compression Asymmetry in Additive Manufactured Face Centered Cubic High Entropy alloy. *Scripta Materialia* 129, 30–34. doi:10.1016/j.scriptamat.2016.10.023

Khakurel, H., Taufique, M. F. N., Roy, A., Balasubramanian, G., Ouyang, G., Cui, J., et al. (2021). Machine Learning Assisted Prediction of the Young's Modulus of Compositionally Complex Alloys. *Sci. Rep.* 11 (1), 1–10. doi:10.1038/S41598-021-96507-0

Kozeschnik, E., and Buchmayr, B. (2001). MatCalc - A Simulation Tool for Multicomponent Thermodynamics, Diffusion and Phase Transformations. *Math. Model. Weld Phenomena* 5, 349–361.

Kresse, G., and Furthmüller, J. (1996). Efficient Iterative Schemes Forab Initiototal-Energy Calculations Using a Plane-Wave Basis Set. *Phys. Rev. B* 54, 11169–11186. doi:10.1103/PhysRevB.54.11169

Kresse, G., and Joubert, D. (1999). From Ultrasoft Pseudopotentials to the Projector Augmented-Wave Method. *Phys. Rev. B* 59, 1758–1775. doi:10.1103/PhysRevB.59.1758

Kukshal, V., Patnaik, A., and Bhat, I. K. (2018). Corrosion and thermal Behaviour of AlCr1.5CuFeNi2Tix High-Entropy Alloys. *Mater. Today Proc.* 5, 17073–17079. doi:10.1016/J.MATPR.2018.04.114

Kunce, I., Polanski, M., and Bystrzycki, J. (2014). Microstructure and Hydrogen Storage Properties of a TiZrNbMoV High Entropy alloy Synthesized Using Laser Engineered Net Shaping (LENS). *Int. J. Hydrogen Energ.* 39, 9904–9910. doi:10.1016/j.ijhydene.2014.02.067

Kunce, I., Polanski, M., and Bystrzycki, J. (2013). Structure and Hydrogen Storage Properties of a High Entropy ZrTiVCrFeNi alloy Synthesized Using Laser Engineered Net Shaping (LENS). *Int. J. Hydrogen Energ.* 38, 12180–12189. doi:10.1016/j.ijhydene.2013.05.071

Kunce, I., Polanski, M., Karczewski, K., Plocinski, T., and Kurzydlowski, K. J. (2015). Microstructural Characterisation of High-Entropy alloy AlCoCrFeNi Fabricated by Laser Engineered Net Shaping. *J. Alloys Compd.* 648, 751–758. doi:10.1016/j.jallcom.2015.05.144

Laplanche, G., Kostka, A., Reinhart, C., Hunfeld, J., Eggeler, G., and George, E. P. (2017). Reasons for the superior Mechanical Properties of Medium-Entropy CrCoNi Compared to High-Entropy CrMnFeCoNi. *Acta Materialia* 128, 292–303. doi:10.1016/j.actamat.2017.02.036

Li, B.-S., Marrow, T. J., and Armstrong, D. E. J. (2020a). Measuring the Brittle-To-Ductile Transition Temperature of Tungsten-Tantalum alloy Using Chevron-Notched Micro-cantilevers. *Scripta Materialia* 180, 77–82. doi:10.1016/J.SCRIPTAMAT.2020.01.030

Li, J., Craeghs, W., Jing, C., Gong, S., and Shan, F. (2017). Microstructure and Physical Performance of Laser-Induction Nanocrystals Modified High-Entropy alloy Composites on Titanium alloy. *Mater. Des.* 117, 363–370. doi:10.1016/j.matdes.2016.12.007

Li, J., and Wang, H. M. (2010). Microstructure and Mechanical Properties of Rapid Directionally Solidified Ni-Base Superalloy Rene′41 by Laser Melting Deposition Manufacturing. *Mater. Sci. Eng. A* 527, 4823–4829. doi:10.1016/j.msea.2010.04.062

Li, M., Gazquez, J., Borisevich, A., Mishra, R., and Flores, K. M. (2018). Evaluation of Microstructure and Mechanical Property Variations in AlxCoCrFeNi High Entropy Alloys Produced by a High-Throughput Laser Deposition Method. *Intermetallics* 95, 110–118. doi:10.1016/j.intermet.2018.01.021

Li, N., Huang, S., Zhang, G., Qin, R., Liu, W., Xiong, H., et al. (2019). Progress in Additive Manufacturing on New Materials: A Review. *J. Mater. Sci. Technol.* 35, 242–269. doi:10.1016/j.jmst.2018.09.002

Li, Q., Zhang, H., Li, D., Chen, Z., Wang, F., and Wu, M. (2020b). Comparative Study of the Microstructures and Mechanical Properties of Laser Metal Deposited and Vacuum Arc Melted Refractory NbMoTa Medium-Entropy alloy. *Int. J. Refractory Met. Hard Mater.* 88, 105195. doi:10.1016/j.ijrmhm.2020.105195

Li, R., Wang, M., Yuan, T., Song, B., Chen, C., Zhou, K., et al. (2017c). Selective Laser Melting of a Novel Sc and Zr Modified Al-6.2 Mg alloy: Processing, Microstructure, and Properties. *Powder Technol.* 319, 117–128. doi:10.1016/j.powtec.2017.06.050

Li, W., Liaw, P. K., and Gao, Y. (2018c). Fracture Resistance of High Entropy Alloys: A Review. *Intermetallics* 99, 69–83. doi:10.1016/j.intermet.2018.05.013

López, G. A., Mittemeijer, E. J., and Straumal, B. B. (2004). Grain Boundary Wetting by a Solid Phase; Microstructural Development in a Zn–5 Wt% Al alloy. *Acta Materialia* 52, 4537–4545. doi:10.1016/j.actamat.2004.06.011

Ma, Y., Jiang, B., Li, C., Wang, Q., Dong, C., Liaw, P., et al. (2017). The BCC/B2 Morphologies in AlxNiCoFeCr High-Entropy Alloys. *Metals* 7, 57. doi:10.3390/met7020057

Michopoulos, J. G., Iliopoulos, A. P., Steuben, J. C., Birnbaum, A. J., and Lambrakos, S. G. (2018). On the Multiphysics Modeling Challenges for Metal Additive Manufacturing Processes. *Additive Manufacturing* 22, 784–799. doi:10.1016/j.addma.2018.06.019

Mishra, R. S., Kumar, N., and Komarasamy, M. (2015). Lattice Strain Framework for Plastic Deformation in Complex Concentrated Alloys Including High Entropy Alloys. *Mater. Sci. Technol.* 31, 1259–1263. doi:10.1179/1743284715y.0000000050

Moorehead, M., Bertsch, K., Niezgoda, M., Parkin, C., Elbakhshwan, M., Sridharan, K., et al. (2020). High-throughput Synthesis of Mo-Nb-Ta-W High-Entropy Alloys via Additive Manufacturing. *Mater. Des.* 187, 108358. doi:10.1016/j.matdes.2019.108358

Nartu, M. S. K. K. Y., Alam, T., Dasari, S., Mantri, S. A., Gorsse, S., Siller, H., et al. (2020). Enhanced Tensile Yield Strength in Laser Additively Manufactured Al0.3CoCrFeNi High Entropy alloy. *Materialia* 9, 100522. doi:10.1016/j.mtla.2019.100522

Ocelík, V., Janssen, N., Smith, S. N., and De Hosson, J. T. M. (2016). Additive Manufacturing of High-Entropy Alloys by Laser Processing. *JOM* 68, 1810–1818. doi:10.1007/s11837-016-1888-z

Osei-Agyemang, E., and Balasubramanian, G. (2021). Effect of Oxidation on the thermal Expansion of a Refractory Multicomponent alloy. *Philos. Mag. Lett.* 101, 173–182. doi:10.1080/09500839.2021.1881641

Osei-Agyemang, E., and Balasubramanian, G. (2019). Surface Oxidation Mechanism of a Refractory High-Entropy alloy. *Npj Mater. Degrad.* 3 (1), 1–8. doi:10.1038/S41529-019-0082-5

Ostovari Moghaddam, A., Shaburova, N. A., Samodurova, M. N., Abdollahzadeh, A., and Trofimov, E. A. (2021). Additive Manufacturing of High Entropy Alloys: A Practical Review. *J. Mater. Sci. Technol.* 77, 131–162. doi:10.1016/j.jmst.2020.11.029

Plimpton, S. (1995). Fast Parallel Algorithms for Short-Range Molecular Dynamics. *J. Comput. Phys.* 117, 1–19. doi:10.1006/jcph.1995.1039

Qiu, Z., Yao, C., Feng, K., Li, Z., and Chu, P. K. (2018). Cryogenic Deformation Mechanism of CrMnFeCoNi High-Entropy alloy Fabricated by Laser Additive Manufacturing Process. *Int. J. Lightweight Mater. Manufacture* 1, 33–39. doi:10.1016/j.ijlmm.2018.02.001

Ramakrishnan, A., and Dinda, G. P. (2019). Direct Laser Metal Deposition of Inconel 738. *Mater. Sci. Eng. A* 740-741, 1–13. doi:10.1016/j.msea.2018.10.020

Rickman, J. M., Balasubramanian, G., Marvel, C. J., Chan, H. M., and Burton, M.-T. (2020). Machine Learning Strategies for High-Entropy Alloys. *J. Appl. Phys.* 128, 221101. doi:10.1063/5.0030367

Rickman, J. M., Chan, H. M., Harmer, M. P., Smeltzer, J. A., Marvel, C. J., Roy, A., et al. (2019). Materials Informatics for the Screening of Multi-Principal Elements and High-Entropy Alloys. *Nat. Commun.* 10, 1–10. doi:10.1038/s41467-019-10533-1

Roy, A., Babuska, T., Krick, B., and Balasubramanian, G. (2020). Machine Learned Feature Identification for Predicting Phase and Young's Modulus of Low-, Medium- and High-Entropy Alloys. *Scripta Materialia* 185, 152–158. doi:10.1016/j.scriptamat.2020.04.016

Roy, A., and Balasubramanian, G. (2021). Predictive Descriptors in Machine Learning and Data-Enabled Explorations of High-Entropy Alloys. *Comput. Mater. Sci.* 193, 110381. doi:10.1016/j.commatsci.2021.110381

Roy, A., Munshi, J., and Balasubramanian, G. (2021a). Low Energy Atomic Traps Sluggardize the Diffusion in Compositionally Complex Refractory Alloys. *Intermetallics* 131, 107106. doi:10.1016/j.intermet.2021.107106

Roy, A., Sreeramagiri, P., Babuska, T., Krick, B., Ray, P. K., and Balasubramanian, G. (2021b). Lattice Distortion as an Estimator of Solid Solution Strengthening in High-Entropy Alloys. *Mater. Characterization* 172, 110877. doi:10.1016/j.matchar.2021.110877

Sames, W. J., List, F. A., Pannala, S., Dehoff, R. R., and Babu, S. S. (2016). The Metallurgy and Processing Science of Metal Additive Manufacturing. *Int. Mater. Rev.* 61, 315–360. doi:10.1080/09506608.2015.1116649

Saunders, N., Guo, U. K. Z., Li, X., Miodownik, A. P., and Schillé, J.-P. (2003). Using JMatPro to Model Materials Properties and Behavior. *JOM* 55, 60–65. doi:10.1007/s11837-003-0013-2

Scime, L., and Beuth, J. (2019). Using Machine Learning to Identify Iin-Ssitu Melt Pool Signatures Indicative of Flaw Formation in a Laser Powder Bed Fusion Additive Manufacturing Process. *Additive Manufacturing* 25, 151–165. doi:10.1016/J.ADDMA.2018.11.010

Senkov, O. N., Wilks, G. B., Miracle, D. B., Chuang, C. P., and Liaw, P. K. (2010). Refractory High-Entropy Alloys. *Intermetallics* 18, 1758–1765. doi:10.1016/j.intermet.2010.05.014

Sharma, A., and Balasubramanian, G. (2017). Dislocation Dynamics in Al0.1CoCrFeNi High-Entropy alloy under Tensile Loading. *Intermetallics* 91, 31–34. doi:10.1016/j.intermet.2017.08.004

Sharma, A., Deshmukh, S. A., Liaw, P. K., and Balasubramanian, G. (2017a). Crystallization Kinetics in AlxCrCoFeNi (0 ≤ X ≤ 40) High-Entropy Alloys. *Scripta Materialia* 141, 54–57. doi:10.1016/j.scriptamat.2017.07.024

Sharma, A., Levitas, V. I., Singh, P., Basak, A., Balasubramanian, G., and Johnson, D. D. (2018). *Twinning-induced Pseudoelastic Behavior in (MoW)$_{85}$(TaTi)$_{7.5}$Zr$_{7.5}$*, 7.

Sharma, A., Singh, P., Johnson, D. D., Liaw, P. K., and Balasubramanian, G. (2016). Atomistic Clustering-Ordering and High-Strain Deformation of an Al0.1CrCoFeNi High-Entropy alloy. *Sci. Rep.* 6, 31028. doi:10.1038/srep31028

Sharma, A., Singh, P., Kirk, T., Levitas, V. I., Liaw, P. K., Balasubramanian, G., et al. (2021). Pseudoelastic Deformation in Mo-Based Refractory Multi-Principal Element Alloys. *Acta Materialia* 220, 117299. doi:10.1016/J.ACTAMAT.2021.117299

Sharma, A., Singh, R., Liaw, P. K., and Balasubramanian, G. (2017b). Cuckoo Searching Optimal Composition of Multicomponent Alloys by Molecular Simulations. *Scripta Materialia* 130, 292–296. doi:10.1016/j.scriptamat.2016.12.022

Shen, C., Pan, Z., Ma, Y., Cuiuri, D., and Li, H. (2015). Fabrication of Iron-Rich Fe-Al Intermetallics Using the Wire-Arc Additive Manufacturing Process. *Additive Manufacturing* 7, 20–26. doi:10.1016/j.addma.2015.06.001

Singh, P., Marshal, A., Smirnov, A. V., Sharma, A., Balasubramanian, G., Pradeep, K. G., et al. (2019). Tuning Phase Stability and Short-Range Order through Al Doping in (CoCrFeMn)100−xAlx High-Entropy Alloys. *Phys. Rev. Mater.* 3, 075002. doi:10.1103/PhysRevMaterials.3.075002

Singh, P., Sharma, A., Smirnov, A. V., Diallo, M. S., Ray, P. K., Balasubramanian, G., et al. (2018). Design of High-Strength Refractory Complex Solid-Solution Alloys. *Npj Comput. Mater.* 4, 16. doi:10.1038/s41524-018-0072-0

Singh, R., Sharma, A., Singh, P., Balasubramanian, G., and Johnson, D. D. (2021a). Accelerating Computational Modeling and Design of High-Entropy Alloys. *Nat. Comput. Sci.* 1, 54–61. doi:10.1038/s43588-020-00006-7

Singh, R., Singh, P., Sharma, A., Bingol, O. R., Balu, A., Balasubramanian, G., et al. (2021b). Neural-networks Model for Force Prediction in Multi-Principal-Element Alloys. *arXiv pre-print server*.

Sistla, H. R., Newkirk, J. W., and Frank Liou, F. (2015). Effect of Al/Ni Ratio, Heat Treatment on Phase Transformations and Microstructure of Al FeCoCrNi2−(X= 0.3, 1) High Entropy Alloys. *Mater. Des.* 81, 113–121. doi:10.1016/j.matdes.2015.05.027

Sreeramagiri, P., Bhagavatam, A., Alrehaili, H., and Dinda, G. (2020a). Direct Laser Metal Deposition of René 108 Single crystal Superalloy. *J. Alloys Compd.* 838, 155634. doi:10.1016/j.jallcom.2020.155634

Sreeramagiri, P., Bhagavatam, A., Ramakrishnan, A., Alrehaili, H., and Dinda, G. P. (2020b). Design and Development of a High-Performance Ni-Based Superalloy WSU 150 for Additive Manufacturing. *J. Mater. Sci. Technol.* 47, 20–28. doi:10.1016/j.jmst.2020.01.041

Sreeramagiri, P., Roy, A., and Balasubramanian, G. (2021). Effect of Cooling Rate on the Phase Formation of AlCoCrFeNi High-Entropy Alloy. *J. Phase Equilib. Diffus.* 42, 772–780. doi:10.1007/S11669-021-00918-5

Stawovy, M. T. (2018). Comparison of LCAC and PM Mo Deposited Using Sciaky EBAM. *Int. J. Refractory Met. Hard Mater.* 73, 162–167. doi:10.1016/j.ijrmhm.2018.02.009

Straumal, B. B., Gornakova, A. S., Kogtenkova, O. A., Protasova, S. G., Sursaeva, V. G., and Baretzky, B. (2008). Continuous and Discontinuous Grain-Boundary Wetting inZnxAl1−x. *Phys. Rev. B* 78, 054202. doi:10.1103/physrevb.78.054202

Straumal, B. B., Gornakova, A. S., Kucheev, Y. O., Baretzky, B., and Nekrasov, A. N. (2012). Grain Boundary Wetting by a Second Solid Phase in the Zr-Nb Alloys. *J. Materi Eng. Perform.* 21, 721–724. doi:10.1007/s11665-012-0158-7

Tong, Z., Ren, X., Jiao, J., Zhou, W., Ren, Y., Ye, Y., et al. (2019). Laser Additive Manufacturing of FeCrCoMnNi High-Entropy alloy: Effect of Heat Treatment on Microstructure, Residual Stress and Mechanical Property. *J. Alloys Compd.* 785, 1144–1159. doi:10.1016/j.jallcom.2019.01.213

Wang, C., Yu, Y., Zhang, H., Xu, L., Ma, X., Wang, F., et al. (2021). Microstructure and Corrosion Properties of Laser Remelted CrFeCoNi and CrMnFeCoNi High Entropy Alloys Coatings. *J. Mater. Res. Technol.* 15, 5187–5196. doi:10.1016/j.jmrt.2021.10.042

Wang, F. J., Zhang, Y., and Chen, G. L. (2009). Atomic Packing Efficiency and Phase Transition in a High Entropy alloy. *J. Alloys Compd.* 478, 321–324. doi:10.1016/j.jallcom.2008.11.059

Wang, R., Zhang, K., Davies, C., and Wu, X. (2017). Evolution of Microstructure, Mechanical and Corrosion Properties of AlCoCrFeNi High-Entropy alloy Prepared by Direct Laser Fabrication. *J. Alloys Compd.* 694, 971–981. doi:10.1016/j.jallcom.2016.10.138

Welk, B. A., Williams, R. E. A., Viswanathan, G. B., Gibson, M. A., Liaw, P. K., and Fraser, H. L. (2013). Nature of the Interfaces between the Constituent Phases in the High Entropy alloy CoCrCuFeNiAl. *Ultramicroscopy* 134, 193–199. doi:10.1016/j.ultramic.2013.06.006

Wohlers, T., and Tim, G. (2014). History of Additive Manufacturing. *Wohlers Rep.* 24, 118.

Xiang, S., Li, J., Luan, H., Amar, A., Lu, S., Li, K., et al. (2019a). Effects of Process Parameters on Microstructures and Tensile Properties of Laser Melting Deposited CrMnFeCoNi High Entropy Alloys. *Mater. Sci. Eng. A* 743, 412–417. doi:10.1016/j.msea.2018.11.110

Xiang, S., Luan, H., Wu, J., Yao, K.-F., Li, J., Liu, X., et al. (2019b). Microstructures and Mechanical Properties of CrMnFeCoNi High Entropy Alloys Fabricated Using Laser Metal Deposition Technique. *J. Alloys Compd.* 773, 387–392. doi:10.1016/j.jallcom.2018.09.235

Yao, J., Weng, Z., Dong, G., and Yang, L. (2018). Microstructure and Hardness of FeCrNiCoMn High-Entropy alloy Coating Prepared by Laser Cladding with Pre-alloyed Gas Atomized Powder. *Int. Congress Appl. Lasers Electro-Optics* 480, 5062919. doi:10.2351/1.5062919

Yeh, J.-W., Chen, S.-K., Lin, S.-J., Gan, J.-Y., Chin, T.-S., Shun, T.-T., et al. (2004). Nanostructured High-Entropy Alloys with Multiple Principal Elements: Novel Alloy Design Concepts and Outcomes. *Adv. Eng. Mater.* 6, 299–303. doi:10.1002/adem.200300567

Yue, T. M., Xie, H., Lin, X., Yang, H. O., and Meng, G. H. (2014). Solidification Behaviour in Laser Cladding of AlCoCrCuFeNi High-Entropy alloy on Magnesium Substrates. *J. Alloys Compd.* 587, 588–593. doi:10.1016/j.jallcom.2013.10.254

Zhang, M., Parnell, A., Brabazon, D., and Benavoli, A. (2021). *Bayesian Optimisation for Sequential Experimental Design with Applications in Additive Manufacturing*.

Conflict of Interest: The authors declare that the research was conducted in the absence of any commercial or financial relationships that could be construed as a potential conflict of interest.